

Extreme sensitivity biosensing platform based on hyperbolic metamaterials

Kandammathe Valiyaveedu Sreekanth^{1*}, Yunus Alapan², Mohamed ElKabbash¹, Efe Ilker¹, Michael Hinczewski¹, Umut A. Gurkan^{2,3,4,5}, Antonio De Luca⁶ and Giuseppe Strangi^{1,6*}

Optical sensor technology offers significant opportunities in the field of medical research and clinical diagnostics, particularly for the detection of small numbers of molecules in highly diluted solutions. Several methods have been developed for this purpose, including label-free plasmonic biosensors based on metamaterials. However, the detection of lower-molecular-weight (<500 Da) biomolecules in highly diluted solutions is still a challenging issue owing to their lower polarizability. In this context, we have developed a miniaturized plasmonic biosensor platform based on a hyperbolic metamaterial that can support highly confined bulk plasmon guided modes over a broad wavelength range from visible to near infrared. By exciting these modes using a grating-coupling technique, we achieved different extreme sensitivity modes with a maximum of 30,000 nm per refractive index unit (RIU) and a record figure of merit (FOM) of 590. We report the ability of the metamaterial platform to detect ultralow-molecular-weight (244 Da) biomolecules at picomolar concentrations using a standard affinity model streptavidin-biotin.

Plasmonic biosensors allow the rapid detection of biomolecular interactions in real time, which is particularly valuable for the diagnosis of diseases and routine point-of-care (POC) clinical evaluations^{1–16}. The basic principle of the plasmonic sensing mechanism is the excitation of charge density oscillations (surface plasmons) propagating along the metal/dielectric interface when the wavevector of incident light satisfies the resonant condition¹⁷. At visible and near infrared (NIR) wavelengths, the electric field associated with these oscillations is highly sensitive to the change in refractive index of its surrounding medium, and decays exponentially. Plasmonic sensors therefore facilitate the real-time monitoring of biomolecular binding events and can be used to study the nature of such interactions.

There are two classes of conventional plasmonic sensors, based on surface plasmon polaritons (SPPs) and localized surface plasmons (LSPs; ref. 18). Both SPP and LSP sensors measure the sensitivity of the plasmon resonant frequency to small changes in refractive index adjacent to the metal/dielectric interface. SPP sensors are usually built in a Kretschmann configuration that matches momentum between the surface plasmon and a laser beam, whereas LSP sensors exhibit a tunable resonant frequency that does not require momentum matching. LSP sensors geometrically confine electromagnetic energy absorbed from large optical cross-sections to significantly enhance local fields within 5–15 nm of the nanoparticle surface. Although reported sensitivities for LSP sensors are $\approx 2 \times 10^2$ nm/RIU (refs 19,20), due largely to the smaller plasmon-active adsorptive surfaces of nanoparticles relative to planar films, detection levels are comparable to SPP sensors for single-molecule binding events²¹. However, SPP sensors benefit from a high sensitivity to refractive index changes of $\approx 2 \times 10^6$

response units per RIU for a defined planar gold film area and surface coverage by a particular analyte²². On the other hand, LSP-based sensors perform well in some instances, particularly for smaller molecule detection, by precisely tracking the local refractive index changes due to biomolecular reactions by using the concept of optical phase flips¹¹. Recent progress in microfabrication and nanofabrication has encouraged the development of novel label-free plasmonic biosensors, particularly metamaterials, which can overcome the limitations of conventional plasmonic sensors^{12–14,23–26}. A metamaterial based on two-dimensional (2D) porous gold nanorod arrays has also been proposed for high-sensitivity plasmonic biosensors¹⁴. The reported sensitivity was 30,000 nm per RIU, with a maximum probe depth of 500 nm at NIR frequencies. However, plasmonic nanorod metamaterials show enhanced sensitivity solely in the infrared spectral region, and the sensing mechanism remains based on the bulk Kretschmann configuration. Even though this configuration is miniaturized for commercial biosensing, it is not suitable for POC applications owing to the bulky high-end instruments of the Kretschmann configuration¹⁶. In addition, a higher figure of merit (FOM) and ultrahigh sensitivity are required to detect small numbers of lower-molecular-weight (<500 Da) biomolecules, such as proteins, hormones and drugs, owing to their lower polarizability, which decreases the resonance shift of the sensor.

To address the drawbacks of current plasmonic biosensors, we have developed a plasmonic biosensor platform based on hyperbolic metamaterials (HMMs) that demonstrates broadband extreme sensitivity from visible to NIR wavelengths. HMMs are unusual electromagnetic metamaterials that feature hyperbolic dispersion because one of their principal components has the

¹Department of Physics, Case Western Reserve University, 10600 Euclid Avenue, Cleveland, Ohio 44106, USA. ²Case Biomanufacturing and Microfabrication Laboratory, Mechanical and Aerospace Engineering Department, Case Western Reserve University, Cleveland, Ohio 44106, USA.

³Biomedical Engineering Department, Case Western Reserve University, Cleveland, Ohio 44106, USA. ⁴Department of Orthopedics, Case Western Reserve University, Cleveland, Ohio 44106, USA. ⁵Advanced Platform Technology Center, Louis Stokes Cleveland Veterans Affairs Medical Center, Cleveland, Ohio 44106, USA. ⁶CNR-NANOTEC Istituto di Nanotecnologia and Department of Physics, University of Calabria, 87036-Rende, Italy.

*e-mail: sreekanth3@gmail.com; giuseppe.strangi@case.edu

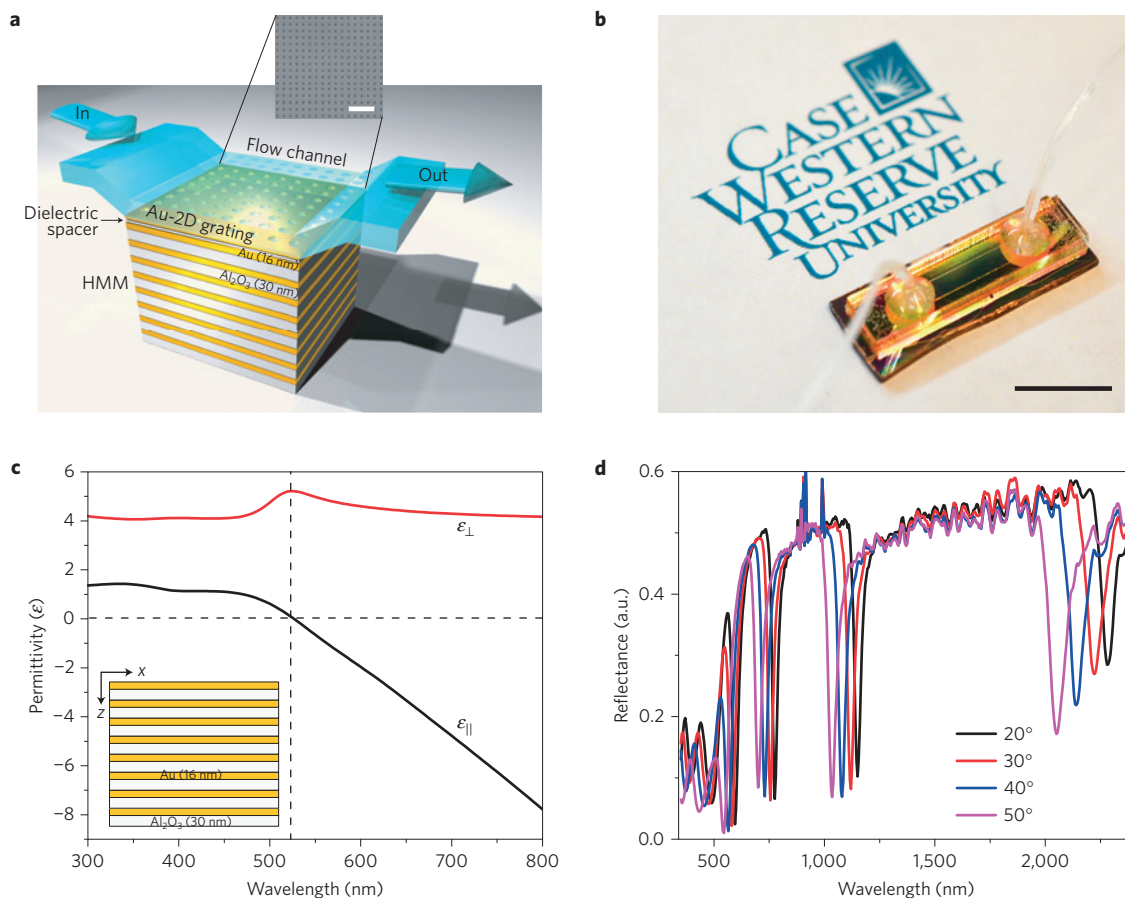


Figure 1 | Fabrication and characterization of a metamaterial sensor device integrated with microfluidics. **a**, A schematic representation of the fabricated miniaturized GC-HMM sensor device with a fluid flow channel and a SEM image of the fabricated 2D subwavelength gold diffraction grating on top of the HMM with an average period of 500 nm and hole size of 160 nm (scale bar, 2 μm). **b**, Photograph of the GC-HMM sensor device fully integrated with a microfluidic channel and sample tubing. Scale bar, 10 mm. **c**, Real parts of effective permittivity of gold/ Al_2O_3 HMM determined using effective media theory, which shows a hyperbolic dispersion at $\lambda \geq 520$ nm (dashed vertical line). The experimentally obtained permittivity values of gold and Al_2O_3 were used in these calculations. The fabricated eight pairs of gold/ Al_2O_3 HMMs are shown in the inset. **d**, Reflectance spectra of the GC-HMM at different angles of incidence. The GC-HMM sample shows four prominent reflectance dips, corresponding to the bulk plasmon polariton modes, and two weak reflectance minima in the shorter wavelengths, corresponding to the SPP modes. A blue shift in resonance wavelength with increasing angle of incidence shows all six modes are guided modes.

opposite sign to the other two²⁷. Their properties include the strong enhancement of spontaneous emission^{28,29}, diverging density of states³⁰, negative refraction^{31,32}, biosensing¹⁴ and enhanced superlensing effects³³. HMMs have many promising applications based on their high- k modes, a concept that has been theoretically and experimentally investigated by many research groups^{29,34,35}. We recently reported that the excitation of high- k modes in a planar HMM is possible using a grating-coupling technique^{36–38}. In particular, we propose that HMM geometries coupled to unconventional 2D gold diffraction gratings could be used to realize high-sensitivity biosensors that operate at visible and NIR frequencies simultaneously. A distinct advantage of this geometry is that the spectral position of the resonance can be tuned from visible to NIR by changing both the HMM and the diffraction grating parameters. Because the proposed configuration is based on a grating-coupling technique, the practical realization of a miniaturized and multiplexed sensor device is possible for a wide range of applications, including POC.

Fabrication and characterization of the sensor device

The fabricated HMM multilayer is shown in the inset of Fig. 1c, which comprises 16 alternating thin films of gold and aluminium dioxide (Al_2O_3) (see Methods). The measured thicknesses are 30

and 16 nm for Al_2O_3 and gold, respectively. Because the individual metal and dielectric layer dimensions satisfy the criteria of effective medium theory³⁹ (EMT) and thus achieve homogeneity, the uniaxial dielectric tensor components of an anisotropic gold- Al_2O_3 HMM are evaluated using EMT. The experimentally determined optical constants of gold and Al_2O_3 (Supplementary Fig. 1) were used to determine the uniaxial dielectric tensor components ($\epsilon_{\parallel} = \epsilon_x = \epsilon_y$ and $\epsilon_{\perp} = \epsilon_z$) as shown in Fig. 1c. The fabricated HMM showed a hyperbolic dispersion at $\lambda \geq 520$ nm, where $\epsilon_{\parallel} < 0$ and $\epsilon_{\perp} > 0$. A clear signature showing the presence of high- k modes was obtained by studying the lifetimes of short-lived excitonic states of the chromophores placed in close proximity to the gold/ Al_2O_3 multilayers in both elliptical and hyperbolic bands (Supplementary Fig. 2).

A well-known grating-coupling technique was used to excite the high- k modes of the fabricated HMMs (ref. 36). A metallic diffraction grating was placed on top of the HMM, making it possible to diffract light and produce a wide range of wavevectors entering the HMM (ref. 40). A metallic diffraction grating-coupled HMM (GC-HMM) was fabricated by first depositing a thin (10 nm) Al_2O_3 spacer layer on the HMM (see Methods). A thin dielectric spacer layer can improve the coupling between the diffraction grating and the HMM. Gold can be functionalized with biomolecules easily using thiol-based surface chemistry⁴¹, and

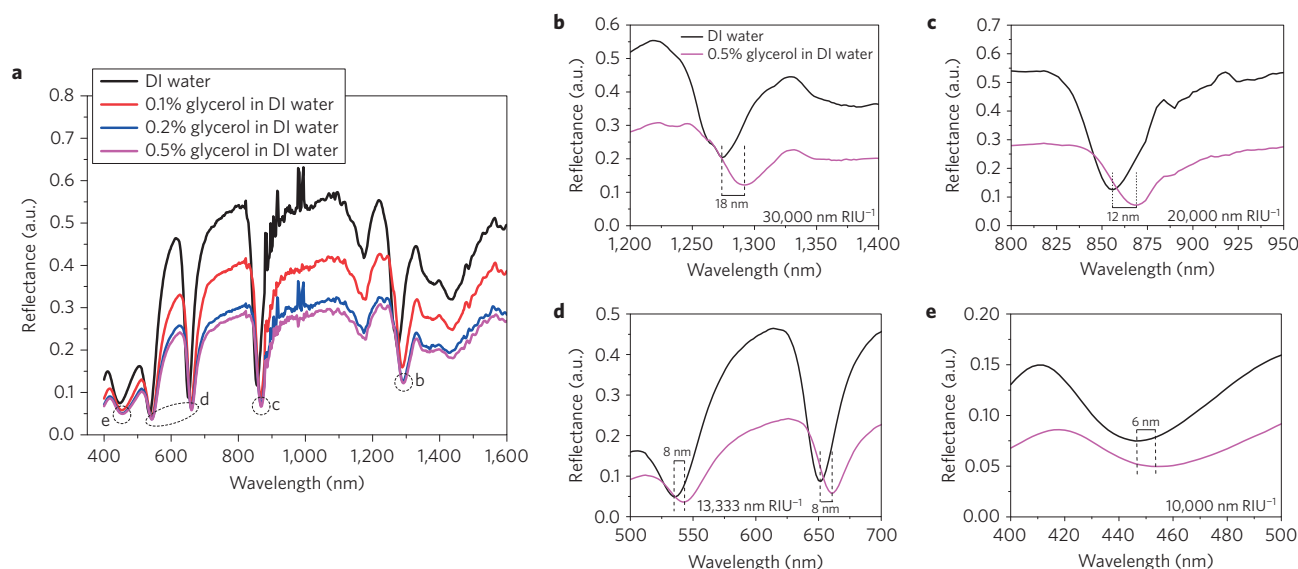


Figure 2 | Sensor calibration test results. **a**, Experimentally obtained reflectance spectra of the sensor device obtained by injecting different weight percentage concentrations of glycerol in distilled (DI) water. A red shift in resonance wavelength is observed when the glycerol weight percentage increases. **b–e**, Enlarged plots of the reflectance spectra (at the positions indicated in **a**) for distilled water and 0.5% glycerol in distilled water of four BPP modes and one SPP mode. The wavelength spectroscopic resolution is set to 1 nm.

here we fabricated gold diffraction gratings. A scanning electron microscope image of a 2D gold diffraction grating on top of a gold/ Al_2O_3 HMM is shown in Fig. 1a. Many grating squares ($100\ \mu\text{m} \times 100\ \mu\text{m}$) with an average period of 500 nm and an average hole diameter of 160 nm were achieved.

For transverse magnetic polarized light, the reflectance spectra of the grating-coupled HMM at different angles of incidence are shown in Fig. 1d. Four reflectance minima with high-quality-factor resonances were obtained in the hyperbolic region ($\lambda > 520\ \text{nm}$) representing the highly confined bulk plasmon polaritons (BPPs). However, two weak reflectance minima were observed in the elliptical region ($\lambda < 500\ \text{nm}$) representing SPPs or long-range surface plasmons of the HMM, given that metal/dielectric stacks support all these modes^{35,36}. Each of the modes was blue-shifted when the angle of incidence increased, indicating that all six modes are guided modes. Because all the modes of GC-HMM behave differently for angle of incidence, we designed and fabricated a biosensor geometry to exploit the extraordinary properties of these modes. The operational principle of our sensor device is based on the coupling condition between grating surface modes and high- k modes. The coupling condition varies when the refractive index of the surrounding medium changes, because the BPPs represent the entire family gap plasmon modes of the metal–dielectric multilayer. This change is observed as a resonant wavelength shift in the reflectance spectrum. A flow microchannel-based miniaturized biosensor platform (Fig. 1a) was therefore developed by assembling the microfluidic system on top of the GC-HMM (see Methods). One such biosensor device integrated with the microfluidic channel is shown in Fig. 1b. The reflectance spectrum of the sensor device was modified at longer wavelengths compared to the GC-HMM (Fig. 1d). Specifically, the fourth BPP mode ($\lambda > 2,000\ \text{nm}$) is missing from the spectrum owing to the greater absorption capacity of the relatively thick polymer channel at longer wavelengths (Supplementary Fig. 4).

Evaluation of the sensor device

A standard sensor evaluation method was used for calibration and to determine the detection limit of the sensor device. Aqueous solutions of glycerol with different weight ratios (0.1–0.5%) were manually injected into the sensor flow microchannel using a

syringe (sample volume $14 \times 2 \times 0.05\ \text{mm}^3$) and the corresponding extremely small refractive index change was recorded as a shift in the reflectance spectrum. The reflectance spectra of glycerol with different weight ratios in distilled water are shown in Fig. 2a. A red shift in resonance wavelength occurred when the weight ratio of glycerol changed, and the quality factor of the resonance clearly declined when the glycerol concentration increased. The difference in refractive index between distilled water (1.3330) and 0.5% glycerol (1.3336) is 0.0006 (ref. 42). The wavelength shift and calculated refractive index sensitivity for NIR wavelength modes are 18 nm and 30,000 nm per RIU for the first mode ($\sim 1,300\ \text{nm}$), and 12 nm and 20,000 nm per RIU for the second mode ($\sim 880\ \text{nm}$) (Fig. 2b,c). The corresponding values for the visible wavelength modes are 8 nm and 13,333 nm per RIU for the first mode ($\sim 660\ \text{nm}$) and second mode ($\sim 550\ \text{nm}$), and 6 nm and 10,000 nm per RIU for the third mode ($\sim 450\ \text{nm}$) (Fig. 2d,e). We have performed numerical simulations to demonstrate the different refractive index sensitivities of different modes for the bulk refractive index changes, and found that the simulated behaviour of modes (Supplementary Fig. 18) exactly matches with experimentally realized results (see Supplementary Section 7).

Another key parameter of a sensor device is the FOM, which is defined as $(\Delta\lambda/\Delta n)(1/\Delta\omega)$, where $\Delta\lambda$ is the wavelength shift, Δn is the refractive index change and $\Delta\omega$ is the full-width of the resonant dip at half-maximum. The FOM is a key biosensing parameter that determines the sensitivity with which very small wavelength changes can be measured, by taking into account the sharpness of the resonance¹⁴. Experimentally obtained FOM values of five resonant dips from visible (450 nm) to NIR (1,300 nm) wavelengths were 108, 206, 357, 535 and 590, respectively, whereas the maximum FOM reported previously was 330 (NIR only) obtained using plasmonic nanorod metamaterials¹⁴. However, we achieved a maximum sensitivity of 30,000 nm per RIU and a record FOM of 590 at NIR frequencies, which shows that the novel sensor device has the ability to detect ultralow concentrations of analytes by measuring very small refractive index changes. Although the plasmonic nanorod metamaterials described previously provide almost the same sensitivity at NIR wavelengths, broadband high sensitivity and high FOM values from visible to NIR cannot be achieved with that configuration¹⁴. In the following biosensing

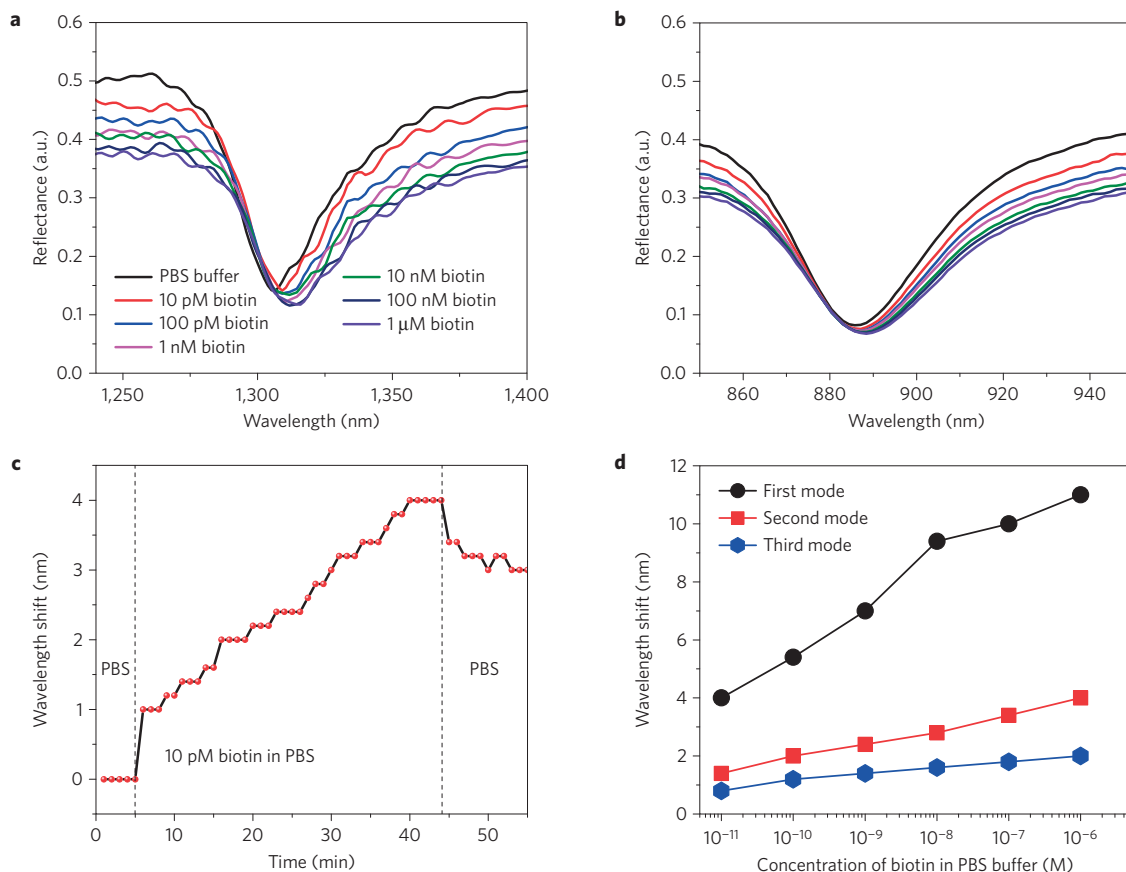


Figure 3 | Evaluation of sensor performance using lower-molecular-weight biomolecules. **a, b**, Reflectance spectra of the sensor device for different concentrations (10 pM to 1 μ M) of biotin in PBS for the first mode (**a**) and the second mode (**b**). **c**, The variation of wavelength shift in the presence of 10 pM biotin in PBS over time. The wavelength spectroscopic resolution is set to 0.2 nm. The wavelength shift shows a distinct red shift over time. **d**, The variation of wavelength shift for three modes with different concentrations of biotin in PBS. The size of the data points in **d** represents the error bar.

experiments, we consider only two NIR wavelength modes (1,300 and 880 nm) and one visible mode (670 nm), because they provide enhanced sensitivity and higher FOM values. These modes are described as the first (1,300 nm), second (880 nm) and third (670 nm) BPPs, respectively.

Detection of lower-molecular-weight biomolecules

To demonstrate the ability of the novel sensor device to detect lower-molecular-weight biomolecules in extremely dilute solutions, we used a standard streptavidin–biotin affinity model¹⁴. Biotin has a molecular weight of 244 Da and conventional surface plasmon resonance-based biosensor techniques require relatively high concentrations of biotin ($\geq 100 \mu\text{M}$) to acquire a detectable response¹⁴. In contrast, previously reported plasmonic nanorod metamaterials were able to detect biotin at concentrations as low as 10 μM using a standard analytical chemistry protocol¹⁴. Notably, we were able to enhance the sensitivity of detection by six orders of magnitude, achieving the quantification of 10 pM biotin in phosphate buffered saline (PBS). The sensor was able to measure the refractive index change caused by the capture of biomolecules at the sensor surface within the microfluidic channel. Sensor performance was monitored as a wavelength shift in the reflectance spectrum by injecting different concentrations of biotin (10 pM to 1 μM) into the sensor microchannel.

We first recorded the reflectance spectrum of the sensor device by injecting PBS, and then injected different concentrations of biotin, and the corresponding reflectance spectra were recorded after a reaction time of 40 min for the first mode (Fig. 3a), second mode (Fig. 3b) and third mode (Supplementary Fig. 5). Compared to

Fig. 2a, the spectral positions of the three modes were slightly red-shifted owing to surface chemistry. Before each injection of a new concentration of biotin, PBS was introduced into the microchannel to remove the unbound and weakly attached biotin molecules. The response of the device during the detection of 10 pM biotin is shown in Fig. 3c (for the first mode). PBS was injected into the microchannel to determine the spectral position of the resonance, and then 10 pM biotin was injected and the resonance wavelength was recorded over the time course of the experiment. We observed a red shift and discrete steps in the resonance wavelength over time, which is due to the 0.2 nm discreteness in the wavelength sensitivity, and the variability in the step size is due to statistical fluctuations where larger or smaller numbers of binding events occur (see Supplementary Sections 4 and 6). Finally, a small blue shift in resonance wavelength was observed by injecting PBS into channel again, to remove the unbound and weakly attached biotin molecules (see Supplementary Fig. 8). The performance of the sensor for the three modes is shown in Fig. 3d, which plots the wavelength shift with different concentrations of biotin (10 pM to 1 μM). Nonlinear variation in the wavelength shift, as a function of the biotin concentration, was observed for all three modes (see Supplementary Section 6). The first mode achieved a greater wavelength shift than the second and third modes because it was most sensitive to the extremely small refractive index change and the maximum FOM.

Demonstration of ultrahigh sensitivity of the sensor

To demonstrate the ultrahigh sensitivity of the sensor device for the detection of biomolecules in extremely dilute solutions without any surface functionalization steps, we used biomolecules of relatively

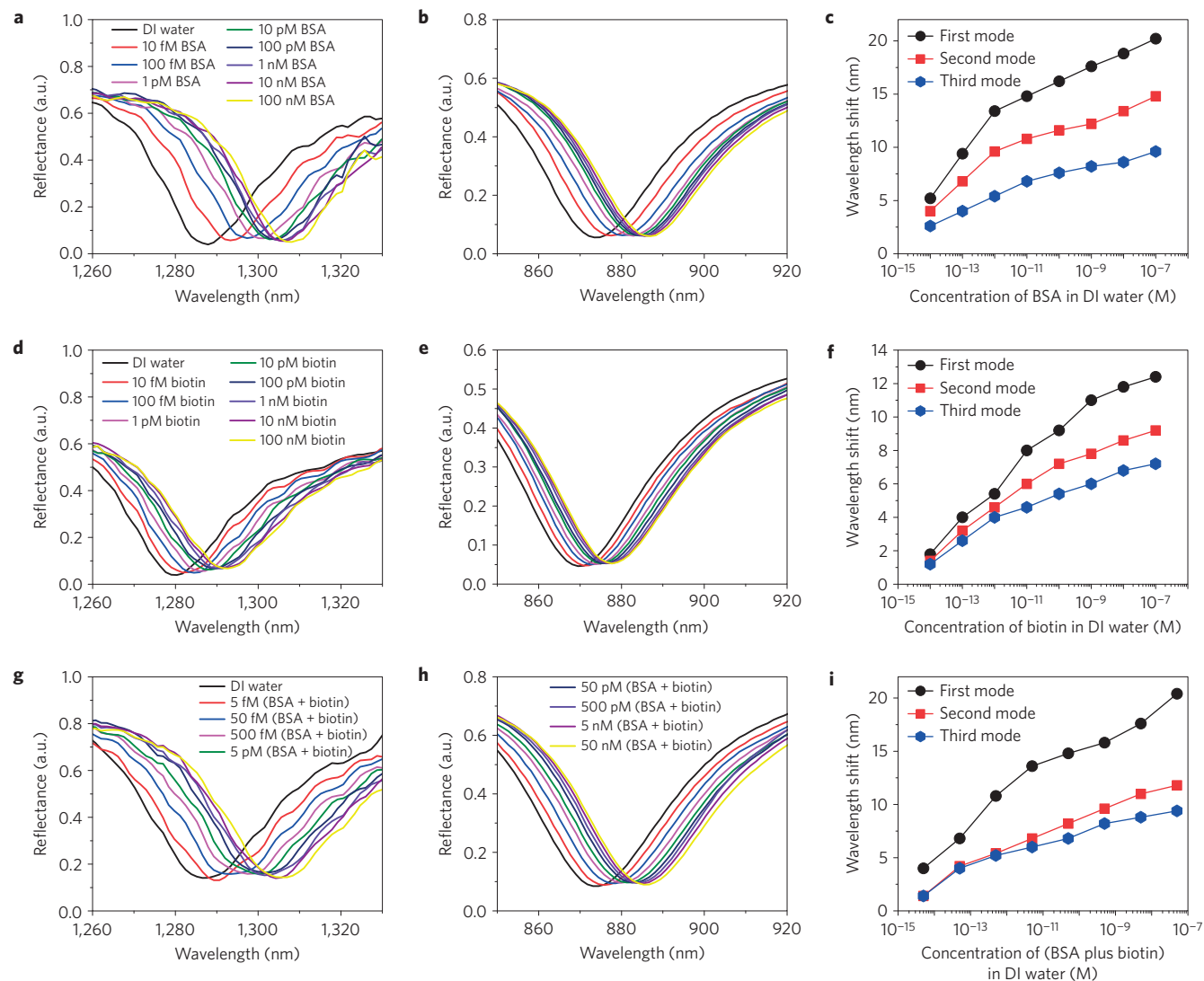


Figure 4 | Evaluation of sensor performance without functionalization. **a,d,g**, Reflectance spectra of the first mode for different concentrations of BSA in distilled water (10 fM to 100 nM) (**a**), biotin in distilled water (10 fM to 100 nM) (**d**) and BSA plus biotin in distilled water (5 fM to 50 nM) (**g**). **b,e,h**, Reflectance spectra of the second mode for different concentrations of BSA in distilled water (10 fM to 100 nM) (**b**), biotin in distilled water (10 fM to 100 nM) (**e**) and BSA plus biotin in distilled water (5 fM to 50 nM) (**h**). **c,f,i**, Variation of the wavelength shift for the three modes with different concentrations of BSA (**c**), biotin (**f**) and BSA plus biotin (**i**) in distilled water. The wavelength spectroscopic resolution is set to 0.4 nm. The size of the data points in **c,f,i**, represents the error bar.

high and low molecular weight—BSA (bovine serum albumin, 66,430 Da) and biotin. Solutions of each molecule prepared in distilled water, with concentrations ranging from 10 fM to 100 nM, were injected into the sensor microchannel (volume = 1.3 μ l) and the wavelength shift of the reflectance spectra was measured. Distilled water was injected into the channel to remove unbound and weakly attached BSA and biotin molecules before each injection of a new solution. The reflectance spectra for highly diluted BSA solutions were recorded after a reaction time of 40 min for the first mode (Fig. 4a), the second mode (Fig. 4b) and the third mode (Supplementary Fig. 12a). In addition, the binding of BSA to the sensor surface (for the first mode) was investigated by recording the wavelength shift of different concentrations of BSA over time (Supplementary Fig. 10). Over the same reaction time, the reflectance spectra for different concentrations of biotin solutions are shown for the first mode (Fig. 4d), second mode (Fig. 4e) and third mode (Supplementary Fig. 12b). The sensor performance for all three modes with different concentrations of BSA and biotin is shown in Fig. 4c,f, respectively. To understand the behaviour of the

wavelength shift with respect to the number of adsorbed particles, we analyse the sensor geometry and the physical details of the adsorption process in Supplementary Section 6. Although we cannot directly measure the population of biomolecules on the sensor surface, we can determine an upper bound on this population, which is on average 84 particles in the long-time limit for the biotin and BSA experiments conducted at 10 fM. Given a first mode shift of 5.2 nm for BSA and 1.8 nm for biotin, this implies a mean shift per particle which is at least 0.06 nm and 0.02 nm respectively. Given the fact that biotin's molecular weight is nearly 300 times smaller than BSA, the relatively small drop in sensitivity going from BSA to biotin is remarkable. Our analysis also revealed that the wavelength shift varies nonlinearly with concentration, decreasing with the number of adsorbed particles on the surface. This nonlinear dependence is described well by a phenomenological double exponential model for both biotin and BSA (Supplementary Fig. 14). The sensor performance is highest at the lowest concentrations. In fact, given the large wavelength shift for BSA at 10 fM, the sensor system should be able to achieve attomolar detection levels.

Remarkably, the wavelength shifts in the first, second and third modes for BSA and biotin behaved differently. Whereas the third mode featured the same wavelength shift for both molecules despite their different molecular weights, the shift in the first mode was greater for BSA than the lighter biotin (Supplementary Fig. 13). It shows that different modes have different sensitivities to different sizes of molecules. To demonstrate this behaviour in detail, we injected different concentrations of mixed solutions of BSA and biotin (5 fM to 50 nM) into the sensor microchannel and recorded the corresponding wavelength shift. The reflectance spectra recorded after a reaction time of 40 min are shown for the first mode (Fig. 4g), second mode (Fig. 4h) and third mode (Supplementary Fig. 12c), and the variation in the wavelength shift with concentration for all three modes is shown in Fig. 4i. We found that the wavelength shift for the first mode was comparable to that of BSA alone, whereas the wavelength shift for third mode was comparable to that of biotin alone. This mode-dependent behaviour of the sensitivity suggests that the nanosensor might be employed as a biological sieve to discriminate binding events of large and small molecules. To justify the physical reasons behind the heterogeneous behaviour of the different modes of GC-HMM, the transversal confinement of different modes in the superstrate (Supplementary Figs 19 and 20) and their sensitivity towards shallow refractive index changes (Supplementary Fig. 21) were numerically simulated and compared with experiment (see Supplementary Section 7). The observation that the different modes are sensitive to the size of the molecules is due to the fact that the transverse decay of the field varies strongly from one mode to another.

Outlook

The ultrahigh sensitivity of the platform reflects the enhanced sensitivity of the GC-HMM for the bulk refractive index change as well as the accumulation of biomolecules on the surface of the 2D subwavelength hole-array grating. The multimodal differential response of our sensor offers a promising opportunity to design an assay for the selective detection of higher- and lower-molecular-weight biomolecules in highly diluted solutions. Both miniaturization and multiplexing are two important features for new generation lab-on-a-chip sensors. Although the miniaturization process of the HMM sensor could reach the fabrication limit of current nano-lithographic techniques (few hundreds of nm), the lateral size is limited from the optical reading cross-section (tens of micrometres), whereas the transversal section would remain in the range of a few hundreds of nanometres. The embedding of the HMM photonic chips in biocompatible matrices (for example, silk) could also allow for transcutaneous implantation. The multiplexing assay is very important in sensing applications because it brings specificity properties to ligand-free sensors and adds specificity features to ligand-functionalized sensors. In particular, the multiplexing properties of the presented HMM sensor are based on the different sensitivities of the BPP modes. This property is harnessed by simultaneously evaluating the overall wavelength shift of all the modes to discriminate binding events of small molecules, which can be detected only from the most sensitive modes, with respect to binding events of large molecules that can be detected by all the modes. This biosensing platform, owing to the sensitivity and the intrinsic multimodal selective response, can be harnessed as an extreme sensitivity biological sieve in real biological samples, to detect ultralow-molecular-weight analytes for routine POC clinical evaluation and real-time diagnosis of diseases. However, multiplex detection is possible for multi-analyte biological samples constituted by molecules whose molecular weight spans at least three orders of magnitude (250 Da–500 kDa). The selective response accuracy is limited by the number of bulk plasmon polariton modes and their relative sensitivity, which ranges between 10,000 and

30,000 nm per RIU. The integration of the metamaterial-based photonic chip with micrometre-sized channels can be adapted to allow microfluidic manipulation of real biological samples, including biochemical operations, amplification by polymerase chain reaction, filtration and blood separation. Furthermore, the biosensing platform can be employed for a wide range of molecule concentrations: from highly diluted concentrations (10 fM) to the more concentrated multi-analyte samples (10 μ M). In summary, we have demonstrated a microfluidics-integrated plasmonic platform based on HMMs for ultrasensitive biosensing. This device has the ability to detect extremely small refractive index changes by exciting the high-k modes associated with HMMs, allowing the detection of lower- and higher-molecular-weight biomolecules in extremely dilute solutions. The sensitivity and FOM of our device largely exceeds current biosensing and chemical sensing technologies. Because the excitation mechanism is based on a grating-coupling technique, the platform could easily be integrated with microfluidic systems for lab-on-a-chip and POC biosensing applications. This miniaturized sensor platform is suitable for the development of next-generation biosensors for high-throughput, label-free, multi-analyte sensing applications.

Methods

Methods and any associated references are available in the [online version of the paper](#).

Received 15 April 2015; accepted 25 February 2016;
published online 28 March 2016

References

- Huang, B., Babcock, H. & Zhuang, X. Breaking the diffraction barrier: super-resolution imaging of cell. *Cell* **143**, 1047–1058 (2010).
- De Angelis, F. *et al.* Breaking the diffusion limit with super-hydrophobic delivery of molecules to plasmonic nanofocusing SERS structures. *Nature Photon.* **5**, 682–687 (2011).
- Zeng, S., Baillargeat, D., Hod, H. E. & Yong, K.-T. Nanomaterials enhanced surface plasmon resonance for biological and chemical sensing applications. *Chem. Soc. Rev.* **43**, 3426–3452 (2014).
- Roy, R., Hohng, S. & Ha, T. A practical guide to single-molecule FRET. *Nature Methods* **5**, 507–516 (2008).
- Poma, A. *et al.* Interactions between saporin, a ribosome-inactivating protein, and DNA: a study by atomic force microscopy. *J. Microsc.* **217**, 69–74 (2005).
- Anker, J. N. *et al.* Biosensing with plasmonic nanosensors. *Nature Mater.* **7**, 442–453 (2008).
- Zijlstra, P., Paulo, P. M. R. & Orrit, M. Optical detection of single non-absorbing molecules using the surface plasmon resonance of a gold nanorod. *Nature Nanotech.* **7**, 379–382 (2012).
- Ament, I. *et al.* Single unlabeled protein on individual plasmonic nanoparticles. *Nano Lett.* **12**, 1092–1095 (2012).
- Acimovic, S. S. *et al.* LSPR chip for parallel, rapid, and sensitive detection of cancer markers in serum. *Nano Lett.* **14**, 2636–2641 (2014).
- Im, H. *et al.* Label-free detection and molecular profiling of exosomes with a nano-plasmonic sensor. *Nature Biotechnol.* **32**, 490–495 (2014).
- Svedendahl, M., Verre, R. & Kall, M. Refractometric biosensing based on optical phase films in sparse and short-range-ordered nanoplasmonic layers. *Light Sci. Appl.* **3**, e220 (2014).
- Wu, C. *et al.* Fano-resonant asymmetric metamaterials for ultrasensitive spectroscopy and identification of molecular monolayers. *Nature Mater.* **11**, 69–75 (2012).
- Kravets, V. G. *et al.* Singular phase nano-optics in plasmonic metamaterials for label-free single-molecule detection. *Nature Mater.* **12**, 304–309 (2013).
- Kabashin, A. V. *et al.* Plasmonic nanorod metamaterials for biosensing. *Nature Mater.* **8**, 867–871 (2009).
- Rodrigo, D. *et al.* Mid-infrared plasmonic biosensing with graphene. *Science* **349**, 165–168 (2015).
- Brolo, A. G. Plasmonics for future biosensors. *Nature Photon.* **6**, 709–713 (2012).
- Raether, H. *Surface Plasmons on Smooth and Rough Surfaces and on Gratings* (Springer, 1988).
- Homola, J., Yee, S. S. & Gauglitz, G. Surface plasmon resonance sensors: review. *Sensors Actuators B* **54**, 3–15 (1999).

19. Chen, H. *et al.* Shape- and size-dependent refractive index sensitivity of gold nanoparticles. *Langmuir* **24**, 5233–5237 (2008).
20. Sannomiya, T. & Voros, J. Single plasmonic nanoparticles for biosensing. *Trends Biotechnol.* **29**, 343–351 (2011).
21. Mayer, K. M. *et al.* A single molecule immunoassay by localized surface plasmon resonance. *Nanotechnology* **21**, 255503 (2010).
22. Roper, D. K., Ahn, W., Taylor, B. & Dall'Asen, A. G. Enhanced spectral sensing by electromagnetic coupling with localized surface plasmons on subwavelength structures. *IEEE Sensors J.* **10**, 531–540 (2010).
23. Liu, N. *et al.* Planar metamaterial analogue of electromagnetically induced transparency for plasmonic sensing. *Nano Lett.* **10**, 1103–1107 (2010).
24. Shen, Y. *et al.* Plasmonic gold mushroom arrays with refractive index sensing figures of merit approaching the theoretical limit. *Nature Commun.* **4**, 2381 (2013).
25. Cao, C. *et al.* Metamaterials-based label-free nanosensor for conformation and affinity biosensing. *ACS Nano* **7**, 7583–7591 (2013).
26. Zeng, S. *et al.* Graphene-gold metasurface architectures for ultrasensitive plasmonic biosensing. *Adv. Mater.* **27**, 6163–6169 (2015).
27. Poddubny, A., Iorsh, I., Belov, P. & Kivshar, Y. Hyperbolic metamaterials. *Nature Photon.* **7**, 948–957 (2013).
28. Lu, D., Kan, J. J., Fullerton, E. E. & Liu, Z. Enhancing spontaneous emission rates of molecules using nanopatterned multilayer hyperbolic metamaterials. *Nature Nanotech.* **9**, 48–53 (2014).
29. Krishnamoorthy, H. N. S. *et al.* Topological transitions in metamaterials. *Science* **336**, 205–209 (2012).
30. Jacob, Z., Smolyaninov, I. I. & Narimanov, E. E. Broadband Purcell effect: radiative decay engineering with metamaterials. *Appl. Phys. Lett.* **100**, 181105 (2012).
31. Hoffman, A. J. *et al.* Negative refraction in semiconductor metamaterials. *Nature Mater.* **6**, 946–950 (2007).
32. Sreekanth, K. V., De Luca, A. & Strangi, G. Negative refraction in graphene-based hyperbolic metamaterials. *Appl. Phys. Lett.* **103**, 023107 (2013).
33. Ono, A., Kato, J. I. & Kawat, S. Subwavelength optical imaging through a metallic nanorod array. *Phys. Rev. Lett.* **95**, 267407 (2005).
34. Zhukovsky, S. V., Kidwai, O. & Sipe, J. E. Physical nature of volume plasmon polaritons in hyperbolic metamaterials. *Opt. Exp.* **21**, 14982–14987 (2013).
35. Avrutsky, I., Salakhutdinov, I., Elser, J. & Podolskiy, V. Highly confined optical modes in nanoscale metal-dielectric multilayers. *Phys. Rev. B* **75**, 241402 (2007).
36. Sreekanth, K. V., De Luca, A. & Strangi, G. Experimental demonstration of surface and bulk plasmon polaritons in hypergratings. *Sci. Rep.* **3**, 3291 (2013).
37. Sreekanth, K. V., De Luca, A. & Strangi, G. Excitation of volume plasmon polaritons in metal-dielectric metamaterials using 1D and 2D diffraction gratings. *J. Opt.* **16**, 105103 (2014).
38. Sreekanth, K. V., Hari Krishna, K., De Luca, A. & Strangi, G. Large spontaneous emission rate enhancement in grating coupled hyperbolic metamaterials. *Sci. Rep.* **4**, 6340 (2014).
39. Cortes, C. L., Newman, W., Molesky, S. & Jacob, Z. Quantum nanophotonics using hyperbolic metamaterials. *J. Opt.* **14**, 063001 (2012).
40. Yan, W., Shen, L., Ran, L. & Kong, J. A. Surface modes at the interfaces between isotropic media and indefinite media. *J. Opt. Soc. Am. A* **24**, 530–535 (2007).
41. Baptista, P. *et al.* Gold nanoparticles for the development of clinical diagnosis methods. *Anal. Bioanal. Chem.* **391**, 943–50 (2008).
42. Weast, R. C. *CRC Handbook of Chemistry and Physics* (CRC Press, 1987).

Acknowledgements

We acknowledge support from the Ohio Third Frontier Project 'Research Cluster on Surfaces in Advanced Materials (RC-SAM) at Case Western Reserve University'. This work was also supported in part by Grant # 2013126 from the Doris Duke Charitable Foundation and by the Italian Project 'NanoLase'-PRIN 2012, protocol number 2012JHFYMC. In addition, we acknowledge the support of the MORE Center at Case Western Reserve University and the GU Malignancies Program of the Case Comprehensive Cancer Center.

Author contributions

K.V.S. and G.S. conceived the idea. K.V.S., Y.A., M.E., U.A.G., A.D.L. and G.S. designed the research. K.V.S. fabricated and characterized the sensor device, performed experiments and carried out numerical simulations. Y.A. fabricated the microfluidic channels, performed surface chemistry and prepared biologically relevant samples. M.E. performed experiments. E.I. and M.H. developed the theoretical models. K.V.S. and G.S. wrote the manuscript. All authors analysed the data, discussed the results, and edited the manuscript.

Additional information

Supplementary information is available in the [online version of the paper](#). Reprints and permissions information is available online at www.nature.com/reprints. Correspondence and requests for materials should be addressed to K.V.S. or G.S.

Competing financial interests

The authors declare no competing financial interests.

Methods

Chemicals. Glycerol, absolute ethanol, dimethyl sulfoxide (DMSO), lyophilized BSA, the coupling molecule N-g-maleimidobutyryloxysuccinimide ester (GMBS), and (3-mercaptopropyl)trimethoxysilane (3-MPS) were purchased from Sigma Aldrich. PBS (pH 7.4) and D-biotin were purchased from Life Technologies. Neutravidin protein was purchased from Fisher Thermo Scientific. Poly(methylmethacrylate) (PMMA) sheets were purchased from McMaster-Carr.

Device fabrication. HMMs in the form of ultrathin multilayers have several advantages over conventional metamaterials, including three-dimensional (3D) non-resonant optical responses with low loss. HMMs were produced by the sequential deposition of Al_2O_3 and gold layers on a glass substrate (Micro slides, Corning) using electron-beam (e-beam) evaporation of Al_2O_3 pellets and thermal evaporation of gold pellets (both from Kurt J. Lesker). The deposition rate of both materials was 0.3 \AA s^{-1} . A 2D gold diffraction grating was deposited on top of the HMM by e-beam lithography (Tescan Vega). Deep subwavelength gratings were produced using a two-layer photoresist coating. Initially, a methyl methacrylate (MMA) resist (8.5MMAEL 11, MICROCHEM) was spin-coated on the sample at 4,000 r.p.m. and baked at 180°C for 5 min. A PMMA resist (950PMMA C2 Resist, MICROCHEM) was later spin-coated at 5,000 r.p.m. and baked at 180°C for 8 min. The prepared sample was patterned by e-beam lithography at a dosage of 150 mC cm^{-2} and a beam intensity of 8. The exposed samples were developed using methyl isobutyl ketone (MIBK) (isopropyl alcohol (IPA) solution for 90 s and IPA for 30 s) before imaging by scanning electron microscopy (SEM, Tescan Vega), confirming that the periodic holes matched the design precisely. Because the spacer layer is very thin, it is not possible to etch the 2D hole array through the spacer layer to obtain a deep grating. Therefore, we directly deposited a thin (20 nm) gold layer on top of the sample using thermal evaporation of gold pellets as above to realize a metallic diffraction grating. The prepared samples were again imaged by SEM to confirm the uniformity of the gold layer on the gratings.

Microfluidic channel fabrication and integration with the GC-HMM substrate. Microfluidic channels comprised a poly(methyl methacrylate) plastic top (encompassing micromachined inlets and outlets) and a double-sided 50- μm adhesive film defining the outlines and thickness of the microchannels.

PMMA caps were prepared by laser micromachining an inlet and outlet (diameter 0.61 mm, separation 12.4 mm) using a VersaLASER system (Universal Laser Systems). Double-sided adhesive film (iTapestore) was machined to encompass the PMMA component and $14 \times 2 \text{ mm}$ microchannels 50 μm in height. The film was attached to the PMMA component to include the inlet and outlet between the outline of the channels. The GC-HMM substrate was then assembled with the PMMA-film structure to form microfluidic channels within the sensing device.

Optical characterization and experiments. Variable-angle high-resolution spectroscopic ellipsometry (J. A. Woollam, V-VASE) was used to determine the thicknesses and optical constants of the gold and Al_2O_3 thin films. The reflectivity spectra as a function of excitation wavelengths were acquired using the same instrument, with wavelength spectroscopic resolutions of 0.4 nm and 0.2 nm.

Biosample preparation. Glycerol solutions with weight percentage concentrations of 0.1–0.5% were prepared in distilled water. BSA and biotin solutions with varying concentrations (10 μM to 1 mM) were prepared by serial dilution in distilled water (1:10). Biotin solutions (10 pM to 1 mM) were also prepared by serial dilution in PBS (1:10). GMBS stock solution was prepared by dissolving 25 mg GMBS in 0.25 ml DMSO and the stock solution was diluted in ethanol to obtain a 0.28% v/v GMBS working solution. A 4% (v/v) solution of 3-MPS was prepared in ethanol. Neutravidin (1 mg ml^{-1}) was prepared by dissolving 10 mg of the protein in 1 ml distilled water and then diluting in PBS (1:10).

Surface chemistry. The GC-HMM substrates were cleaned using an ultraviolet ozone cleaner (Novascan PSDP-UV8T) for 5 min at 60°C , immediately dipped in ethanol, and then immersed in 3-MPS solution for 30 min at room temperature. The GC-HMM substrates were then dipped in ethanol and immersed in GMBS solution for 15 min at room temperature. The substrates were then dipped in ethanol and distilled water before drying under nitrogen. The microfluidic channels were then joined to inlet and outlet tubes and the channels were flushed with PBS. Neutravidin solution was then injected into the microchannels and incubated for 45 min at room temperature before flushing again with PBS to remove excess neutravidin.